

Calibration Method of Spacecraft–Inertial Sensor Center-of-Mass Offset for the Taiji Gravitational Wave Detection Mission under Science Mode

Haoyue Zhang,^{1,2} Dong Ye,^{1,*} Peng Xu,^{2,3,4,†} Li-E Qiang,⁵ and Ziren Luo²

¹*State Key Laboratory of Micro-Spacecraft Rapid Design and Intelligent Cluster, Harbin Institute of Technology, Harbin 150001, China*

²*Center for Gravitational Wave Experiment, Institute of Mechanics, Chinese Academy of Sciences, Beijing 100190, China*

³*Hangzhou Institute for Advanced Study, University of Chinese Academy of Sciences, Hangzhou 310024, China*

⁴*Lanzhou Center of Theoretical Physics, Lanzhou University, Lanzhou 730000, China*

⁵*National Space Science Center, Chinese Academy of Sciences, Beijing 100190, China*

(Dated: December 24, 2025)

Accurately calibrating the center-of-mass (CoM) offset between the spacecraft (SC) and the inertial sensor test mass (TM) is crucial for space-based gravitational-wave (GW) antennas, such as LISA and Taiji. Current calibration methods require additional spacecraft maneuvers that disrupt science data continuity and inter-satellite links, compromising the coherence of gravitational wave signals. Here, we present a maneuver-free calibration scheme that directly estimates the CoM offset vector using only standard science-mode measurements from inertial sensors, interferometers, and differential wavefront sensors. By embedding the CoM offset induced coupling acceleration as an extended state in a model-based adaptive Kalman filter, we achieve estimation accuracy of 0.01–1.5 mm across all axes with a maximum error below 1%. This approach enables continuous, high-precision calibration during nominal observation runs, ensuring continuous and coherent gravitational wave data collection while maintaining the required precision, and also facilitating advanced DFACS functions such as performance evaluations and fault diagnosis. For LISA-like missions, where data continuity is paramount for detecting faint gravitational wave signals, this method will enhance scientific output and reliability.

I. INTRODUCTION

The Laser Interferometer Space Antenna (LISA) mission [1] was officially approved by the European Space Agency in January 2024. As the most developed space mission, LISA had motivated various space gravitational wave (GW) detection projects since the 2000s, including DECIGO [2–4], Taiji [5, 6], TainQin [7–9], ASTROD [10, 11] and etc. Compared with the ground-based large interferometers, that the LIGO-Virgo-KAGRA collaboration [12–15], space-borne antennas will be free from Newtonian gradient noises situated near the 10 Hz band and limitations on the baselines. The LISA and the mentioned LISA-like missions will have sensitive frequency bands from 0.1 mHz to 1 Hz and will encompass scientific objectives related to much heavier sources such as coalescing super-massive black holes and extreme-mass-ratio inspirals, and also stochastic GW background from the early Universe.

“The Taiji program in space” is a space-borne GW detection mission of China, released by the Chinese Academy of Sciences in 2016. Following its roadmap [16], the first technology demonstration satellite, that the Taiji-1, was launched in August 2019 and has successfully validated the related key technologies including the high precision inertial sensor (IS, also called GRS, Gravitational Reference Sensor) [17], laser interferometer in

space, drag-free controls and ultra-clean and stable satellite platform [18]. The Taiji mission, as one of the representative LISA-like missions, will launch three spacecraft (SC) to heliocentric orbits, forming a nearly equilateral triangular constellation with armlength $\sim 3 \times 10^6$ km. It is expected that the science operations of LISA and Taiji may overlap in the 2030s and studies of the joint data analysis has already aroused more interest [19–22].

High precision IS are of key payloads for the LISA and Taiji missions. The suspended test mass (TM) of each IS serves as the free-falling reference and also as the end mirror for the inter-satellite interferometers. The relative motions between the TMs induced by incident GWs could be measured precisely by means of the so called time-delay interferometry [23] and therefore give rise to the detection of GW signals. The performance of the IS, or the residual acceleration noises of the TMs relative to the local inertial frame, will directly determine the sensitivity level of the space GW antennas. For the Taiji mission, according to its designed sensitivity and noise budgets, the residual acceleration noise for each TM along the sensitive axis (along with the inter-satellite laser link) of the IS should be $\leq 3 \times 10^{-15}$ m/s²/Hz^{1/2} [24]. Such stringent requirement will be upheld and guaranteed by the Drag-Free and Attitude Control System (DFACS) [25], which monitors in real-time and adjusts actively the relative displacements and attitudes between the SC and the TMs. The DFACS maintains the two TMs on-board each SC in nearly perfect free fall along their sensitive axes, while forcing them to follow the SC for the remaining degrees of freedom (including attitudes) [26]. Given

* yed@hit.edu.cn

† xupeng@imech.ac.cn

the careful control of each SC's attitude and the breathing angle of the movable optical sub-assemblies to ensure stable inter-satellite measurement links, the attitude of the TMs will be maintained to align with the laser links, effectively acting as the free-falling end mirrors of the inter-satellite interferometer.

Extensive studies on the DFACS for LISA-like missions have established a comprehensive model of the relative dynamics of the TMs and SC [27]. Within this model, the relative center-of-mass (CoM) offset between the SC and TM (called the SC–TM CoM offset) constitutes the most significant nonlinear effect and gives rise to an important disturbance to the DFACS. The CoM offset vector and its variations will couple with the angular acceleration and angular velocity of the SC respectively, thereby introducing inertial acceleration noises in the local frame [28]. Such CoM coupled noise will also introduce interference into the performance evaluation of the on-board ISs. For example, in the data analysis work of the LISA Pathfinder, the CoM offset was precisely calibrated, and its influence, that the inertial force noises, was accurately removed in obtaining the expected noise curve [29].

For satellite gravity missions, such as CHAMP [30], GRACE [31], and GFO [32], the onboard IS operated in accelerometer mode, and their readouts provided the necessary measurements of non-gravitational perturbations acting on the corresponding SCs. The CoM coupled effects will produce inertial acceleration noises directly to the measured data, degrading the scientific outputs of satellite missions with accelerometers for measuring non-gravitational orbit perturbations. Therefore, the in situ and accurate calibration of the SC–TM CoM offset is of importance [33] for those missions including GW antennas in space. Take GRACE as a representative example, one performed the CoM calibration by commanding large spacecraft attitude maneuvers with magnetorquers. The attitude jitters and the CoM coupled acceleration signals were measured with star trackers and the accelerometer, and then the offset vector was estimated using the least-squares method [34, 35]. Taiji-1 [36–38] and TianQin-1 (the technology demonstration satellite of TianQin project) [39, 40] adopted the similar maneuver strategy and employed Kalman filtering algorithms to estimate the CoM offset. The feasibility of applying this method to the Taiji mission was studied and verified with numerical simulations [41]. Furthermore, the TianQin team also analyzed the maneuver design criteria for the possible CoM calibration, which could maintain the inter-satellite link at the same time [42]. In short, during their commissioning and calibration phases, the maneuver-based SC–TM CoM offset calibration methods could meet the requirements of the LISA-like missions [41, 43].

During the years-long scientific lifetime of LISA and Taiji, the SC–TM CoM offset vector could change slowly with time, which may be caused by the continuous consumption of the propellant, the structural deformation due to material aging, or the possible drift of the balance

point of the TMs. Therefore, the scheduled CoM calibration in the science operation phase will be necessary in ensuring the quality of scientific data and the accurate assessment of the performance of IS [44]. However, the maneuver-based calibration will cost extra price when the space-borne GW antenna is performing science measurements. The rather large attitude swings (such as the $100 \mu\text{N} \cdot \text{m}$ maneuver proposed in [42]) would consume a substantial portion of the DFACS control margin and severely compromise the stability of the inter-spacecraft laser links. This contradicts the very purpose of using the H_∞ control approach in DFACS to ensure system robustness. More critically, the maneuvers and the resulting coupled acceleration noises would disrupt the continuity of the science data and break the coherence of the GW signals, thereby would increase the difficulty of source parameter estimations and may even affect the final scientific output of the missions.

To meet the CoM offset calibration requirements of the Taiji mission, this paper proposes a maneuver-free scheme applicable during the science run without any disruption to the measurement system. As discussed earlier, the CoM offset induces disturbances that can substantially influence the performance of the DFACS system, which, correspondingly, will be manifested in the readout signals of the DFACS measurement subsystems—namely, the local TM laser interferometer (IFO) [45], differential wavefront sensor (DWS) [46], and IS. These readouts and their correlations make it possible to identify the SC–TM CoM offset vector given the SC–TM dynamical model. We developed a high-fidelity DFACS numerical simulations and generate the synthetic readout data set. By embedding the CoM offset as an extended state, alongside the bias terms and the dominant colored noises, we reformulate this problem as an extended estimation problem that could be solved via an improved Sage–Husa adaptive Kalman filter. The proposed method enables high-precision CoM offset identification directly from unperturbed science-mode data, without requiring auxiliary maneuvers.

This paper expands as follows. Section II introduces the purpose of the DFACS system, describes the physical configuration and operating principle of the IS, and presents the equations governing the SC–TM relative dynamics and spacecraft attitude motion. Section III designs and constructs a DFACS for Taiji to achieve high-precision simulation of the relative attitude/displacement between the SC–TM and the SC attitude signal in the inertial frame under science mode. Section IV presents the CoM calibration methodology, detailing a baseline approach that relies solely on DFACS-provided SC–TM relative displacement data without spacecraft maneuvers. The method is validated using 25 days of high-fidelity DFACS simulation data, and the resulting CoM offset estimates are reported. Finally, Section V concludes the paper and discusses implications for mission operations.

II. SPACECRAFT-TEST MASS DYNAMICS MODEL

Figure 1 illustrates the internal layout configuration of the Taiji spacecraft. For concreteness, SC1, the first spacecraft in the constellation, is used as a representative example. Inside SC1, two TMs undergo free fall along their respective sensing axes, \mathbf{o}_{11} and \mathbf{o}_{12} , which are separated by an angle of 60° . Each TM is enclosed within an electrode cage, rigidly mounted to both the SC and its associated optical bench. The IS employs sensing electrodes in the cage to measure the TM-SC relative displacement, and actuation electrodes to apply electrostatic forces on the TM.

Owing to their shared measurement principle, LISA, Taiji, and TianQin feature highly similar internal mechanical layouts [47]. we adopt the coordinate systems established in [28], which provide consistent frames for expressing forces, torques, and kinematic relationships. The key reference frames illustrated in Figure 1 are defined as follows:

- Heliocentric Inertial Reference Frame (IRF): $\text{IRF} = \{O^I, i_1, i_2, i_3\}$,
- Constellation Reference Frame (CRF): $\text{CRF} = \{O^C, c_1, c_2, c_3\}$, \mathbf{c}_1 is aligned with the bisector of the incoming laser beam directions \mathbf{l}_2 (from SC2) and \mathbf{l}_3 (from SC3); \mathbf{c}_2 lies in the plane spanned by \mathbf{l}_2 and \mathbf{l}_3 , orthogonal to \mathbf{c}_1 , $\mathbf{c}_3 = \mathbf{c}_1 \times \mathbf{c}_2$.
- Spacecraft Reference Frame (SRF): $\text{SRF} = \{O^S, s_1, s_2, s_3\}$.
- Optical Reference Frame of the i -th optical bench (ORF $_i$): $\text{ORF}_i = \{O^{O_i}, o_{1i}, o_{2i}, o_{3i}\}$, for $i = 1, 2$,
- Test-Mass Reference Frame of the i -th TM (MRF $_i$): $\text{MRF}_i = \{O^{m_i}, m_{1i}, m_{2i}, m_{3i}\}$, for $i = 1, 2$.

Specifically, the superscript of a variable or parameter denotes the reference frame in which it is defined, while the subscript indicates the relative relationship or the entities involved in that variable. For example:

$\mathbf{r}_{m_i O_i}^{O_i}$: The relative displacement between the i -th optical platform and the i -th TM in ORF $_i$.

\mathbf{b}_i : The center-of-mass offset vector of the i -th test mass relative to the CoM of SC.

$\mathbf{q}_{SI}, \mathbf{q}_{SC}$: Attitude quaternions of the SC relative to the IRF and CRF, respectively.

$\mathbf{q}_{m_i S}$: Attitude quaternions of the i -th TM relative to the SC.

\mathbf{T}_A^B : The Direction Cosine Matrix (DCM) that represents the coordinate transformation from frame A to frame B.

As the rigorous derivations of DFACS dynamics have been well established in previous studies (e.g., [28, 47]), this paper focuses on the key dynamic relationships essential for controller design and analysis. Specifically, we present: (i) the translational and rotational dynamics of the i -th TM relative to the ORF $_i$ — namely, $\mathbf{r}_{m_i O_i}^{O_i}$ and

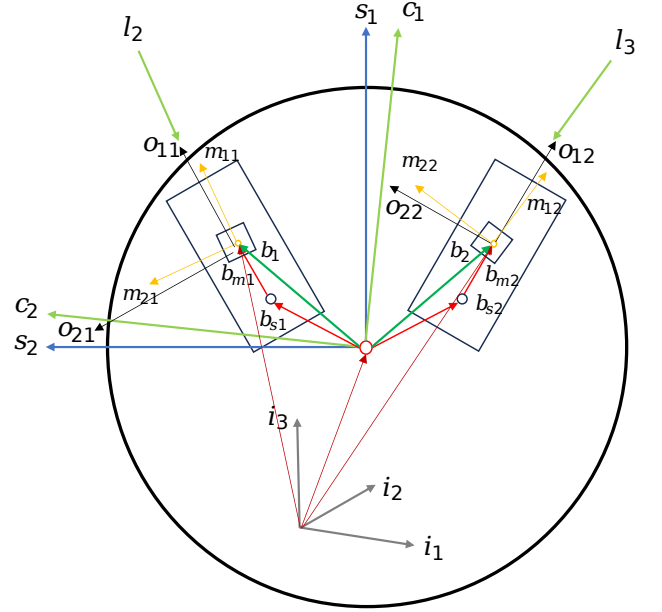


FIG. 1: Reference coordinate system definitions and labeling of key vectors for SC1.

$\mathbf{q}_{m_i O_i}$ — under drag-free control; and (ii) the attitude dynamics of the SC relative to the CRF, described by \mathbf{q}_{SC} , under attitude control.

Accurate modeling of the relative dynamics between the SC and its free-falling TMs is fundamental to the DFACS and CoM calibrations for Taiji. To formulate these dynamics, we begin with the translational dynamics of the SC center of mass in the IRF:

$$\ddot{\mathbf{r}}_{SI}^I = \mathbf{a}_g(\mathbf{r}_{SI}^I) + m_S^{-1} \mathbf{T}_S^I \left(\mathbf{F}_T + \mathbf{d}_S - \sum_{i=1}^2 \mathbf{T}_{O_i}^S \mathbf{F}_{E_i} \right). \quad (1)$$

Here, m_S is the mass of SC, \mathbf{F}_T is the thrust of the micro-propulsion system (MPS), \mathbf{d}_S represents environmental forces, \mathbf{F}_{E_i} is the electrostatic forces used to control the TM, and $\mathbf{a}_g(\mathbf{r}_{SI}^I)$ is the gravitational acceleration experienced by the SC, given by

$$\mathbf{a}_g(\mathbf{r}) = -\frac{\mu_s}{\|\mathbf{r} - \mathbf{r}_{\text{sun}}\|^3} (\mathbf{r} - \mathbf{r}_{\text{sun}}) - \frac{\mu_e}{\|\mathbf{r} - \mathbf{r}_e\|^3} (\mathbf{r} - \mathbf{r}_e), \quad (2)$$

where \mathbf{r}_{sun} and \mathbf{r}_e are the position vectors of the Sun and Earth's mass centers expressed in IRF. μ_s is the solar gravitational constant, μ_e is the Earth's gravitational constant. Similarly, the acceleration of TM in IRF is given by

$$\ddot{\mathbf{r}}_{mI}^I = \mathbf{a}_g(\mathbf{r}_{mI}^I) + m_m^{-1} \mathbf{T}_O^I (\mathbf{F}_E + \mathbf{F}_{\text{st}} + \mathbf{d}_m), \quad (3)$$

where $\mathbf{a}_g(\mathbf{r}_{mI}^I)$ is the gravitational acceleration experienced by TM, m_m is the mass of TM, \mathbf{F}_{st} represents the TM stiffness force, primarily induced by the self-gravity gradient [48]. \mathbf{d}_m denotes other environmental noise on

the TM. Finally, the relative acceleration of the i -th TM with respect to the SC can be expressed as

$$\ddot{\mathbf{r}}_{m_i O_i}^{O_i} = \mathbf{T}_I^{O_i} (\ddot{\mathbf{r}}_{m_i I}^I - \ddot{\mathbf{r}}_{SI}^I - \mathbf{T}_S^I \boldsymbol{\Omega}(\boldsymbol{\omega}_{SI}) \mathbf{b}_i^S), \quad (4)$$

where

$$\boldsymbol{\Omega}(\boldsymbol{\omega}_{SI}) := \boldsymbol{\omega}_{SI}^\times \boldsymbol{\omega}_{SI}^\times + \dot{\boldsymbol{\omega}}_{SI}^\times.$$

$\boldsymbol{\omega}_{SI}^\times$ denotes the skew-symmetric matrix of $\boldsymbol{\omega}_{SI}$ (i.e., $\boldsymbol{\omega}_{SI}^\times \mathbf{v} = \boldsymbol{\omega}_{SI} \times \mathbf{v}$), and \mathbf{b}_i^S is the i -th SC-TM CoM offset expressed in the SRF.

In eq(4), $\boldsymbol{\omega}_{SI}$ represents the angular velocity of the SC relative to the IRF expressed in SRF. Unless otherwise specified, all angular velocities and angular accelerations (e.g., $\boldsymbol{\omega}_{SI}$, $\dot{\boldsymbol{\omega}}_{SI}$) are expressed in their body fixed reference frame; thus, explicit superscripts (e.g., S) are omitted for brevity throughout this work.

The attitude dynamic of the SC relative to the IRF is given by

$$\begin{aligned} \dot{\boldsymbol{\omega}}_{SI} = & \mathbf{J}_S^{-1} (\boldsymbol{\omega}_{SI} \times \mathbf{J}_S \boldsymbol{\omega}_{SI}) \\ & + \mathbf{J}_S^{-1} \left(\mathbf{M}_T + \mathbf{D}_S - \sum_{i=1}^2 \mathbf{T}_{O_i}^S \mathbf{M}_{E_i} \right. \\ & \left. + \sum_{i=1}^2 \mathbf{b}_i^S \times (\mathbf{T}_{O_i}^S \mathbf{F}_{E_i}) \right), \end{aligned} \quad (5)$$

where \mathbf{J}_S is the moment of inertia matrix of the SC, \mathbf{M}_T is the control torque generated by the MPS, \mathbf{D}_S denotes the environmental disturbance torque, and \mathbf{M}_{E_i} represents the electrostatic torque applied on the i -th TM. Based on Eq. (5), the angular acceleration of the SC relative to the CRF can be obtained as

$$\boldsymbol{\omega}_{SC} = \boldsymbol{\omega}_{SI} - \mathbf{T}_C^S \boldsymbol{\omega}_{CI}, \quad (6)$$

$$\dot{\boldsymbol{\omega}}_{SC} = \dot{\boldsymbol{\omega}}_{SI} + \boldsymbol{\omega}_{SC}^\times (\mathbf{T}_C^S \boldsymbol{\omega}_{CI}) - \mathbf{T}_C^S \dot{\boldsymbol{\omega}}_{CI}, \quad (7)$$

where $\boldsymbol{\omega}_{CI}$ is the angular velocity of the CRF relative to the IRF. This angular velocity is obtained by

$$\boldsymbol{\omega}_{CI}^\times = \mathbf{T}_I^C \dot{\mathbf{T}}_I^I. \quad (8)$$

Furthermore, its angular acceleration is given by

$$\dot{\boldsymbol{\omega}}_{CI}^\times = \mathbf{T}_I^C \left(\ddot{\mathbf{T}}_I^I - \dot{\mathbf{T}}_I^I \boldsymbol{\omega}_{CI}^\times \right). \quad (9)$$

Taking SC1 as the reference, let \mathbf{r}_{12}^I and \mathbf{r}_{13}^I denote the position vectors from SC1 to SC2 and SC1 to SC3, respectively, expressed in the IRF. Define the unit vectors

$$\begin{aligned} \hat{\mathbf{r}}_{12} &= \frac{\mathbf{r}_{12}^I}{\|\mathbf{r}_{12}^I\|}, & \hat{\mathbf{r}}_{13} &= \frac{\mathbf{r}_{13}^I}{\|\mathbf{r}_{13}^I\|}, \\ \hat{\mathbf{x}}_C^I &= \frac{\hat{\mathbf{r}}_{12} + \hat{\mathbf{r}}_{13}}{\|\hat{\mathbf{r}}_{12} + \hat{\mathbf{r}}_{13}\|}, & \hat{\mathbf{z}}_C^I &= \frac{\mathbf{r}_{12}^I \times \mathbf{r}_{13}^I}{\|\mathbf{r}_{12}^I \times \mathbf{r}_{13}^I\|}, \\ \hat{\mathbf{y}}_C^I &= \hat{\mathbf{z}}_C^I \times \hat{\mathbf{x}}_C^I, \end{aligned}$$

where $\hat{\mathbf{x}}_C^I$ aligns with the bisector of the formation (outward-pointing), $\hat{\mathbf{z}}_C^I$ is normal to the orbital plane, and $\hat{\mathbf{y}}_C^I$ completes the right-handed orthonormal basis. Then, \mathbf{T}_C^I is given by

$$\mathbf{T}_C^I = [\hat{\mathbf{x}}_C^I, \hat{\mathbf{y}}_C^I, \hat{\mathbf{z}}_C^I]. \quad (10)$$

The attitude dynamic of the TM relative to the IRF is given by

$$\dot{\boldsymbol{\omega}}_{mI} = \mathbf{J}_m^{-1} (\boldsymbol{\omega}_{mI}^\times \mathbf{J}_m \boldsymbol{\omega}_{mI}) + \mathbf{J}_m^{-1} (\mathbf{M}_E + \mathbf{D}_m + \mathbf{M}_{st}), \quad (11)$$

where \mathbf{J}_m is the inertia matrix of TM, \mathbf{M}_{E_i} is the electrostatic control torque (appears in Eq. (5)), \mathbf{D}_{m_i} denotes environmental disturbance torques, and \mathbf{M}_{st} is the stiffness torque on the TM (analogous to the structural force $\mathbf{F}_{st,i}$ in Eq. (3)). Based on Eq. (11), the angular velocity and angular acceleration of the i -th TM relative to the SC are obtained as

$$\boldsymbol{\omega}_{m_i O_i} = \boldsymbol{\omega}_{m_i I} - \mathbf{T}_S^{m_i} \boldsymbol{\omega}_{SI}, \quad (12)$$

$$\dot{\boldsymbol{\omega}}_{m_i O_i} = \dot{\boldsymbol{\omega}}_{m_i I} + \boldsymbol{\omega}_{m_i O_i}^\times \mathbf{T}_S^{m_i} \boldsymbol{\omega}_{SI} - \mathbf{T}_S^{m_i} \dot{\boldsymbol{\omega}}_{SI}. \quad (13)$$

III. DRAG-FREE AND ATTITUDE CONTROL DESIGN AND SIMULATION RESULTS

A. Controller design

Building upon the control requirements and SC-TM dynamics established in Sections I and II, this work adopts the DFACS architecture proposed by [49] as the baseline design.

To ensure robust performance when confronted with environmental disturbances and model uncertainties during science operations, a H_∞ control framework is employed for DFACS synthesis. This approach has been extensively applied to different space-borne GW mission concepts, including LISA, Taiji, TIANQIN and etc., and has evolved into a flight-proven design paradigm with demonstrated resilience under realistic mission constraints. Its performance has been conclusively demonstrated by technology demonstration satellites such as LISA Pathfinder [29] which achieved drag-free and attitude control performance at the nm/ $\sqrt{\text{Hz}}$ and nrad levels, respectively.

The H_∞ control method is a robust synthesis approach rooted in norm-optimal control theory, specifically formulated to ensure closed-loop stability and prescribed performance bounds in the presence of model uncertainties and exogenous disturbances. As illustrated in Figure 2, the generalized plant P represents the controlled dynamics (e.g., SC-TM coupled system), while K denotes the to-be-designed controller. The objective is to synthesize a stabilizing controller K that minimizes the worst-case gain from exogenous inputs \mathbf{w} (e.g., disturbances, sensor noise) to regulated outputs \mathbf{z} (e.g., TM-SC relative motion, attitude error).

This is formalized as the H_∞ norm minimization problem [50]

$$\min_{K \in \mathcal{K}} \|F_\ell(P, K)\|_\infty, \quad (14)$$

where \mathcal{K} is the set of all internally stabilizing controllers, and $F_\ell(P, K)$ denotes the *lower linear fractional transformation* (LFT) mapping $\mathbf{w} \mapsto \mathbf{z}$:

$$F_\ell(P, K) = P_{11} + P_{12}K(I - P_{22}K)^{-1}P_{21}. \quad (15)$$

The generalized plant P is partitioned conformably with the input–output structure as

$$P = \begin{bmatrix} P_{11} & P_{12} \\ P_{21} & P_{22} \end{bmatrix}, \quad \text{where} \quad \begin{bmatrix} \mathbf{z} \\ \mathbf{u} \end{bmatrix} = P \begin{bmatrix} \mathbf{w} \\ \mathbf{y} \end{bmatrix},$$

with \mathbf{u} as the control input and \mathbf{y} as the measured output. Since analytical H_∞ solutions are generally intractable

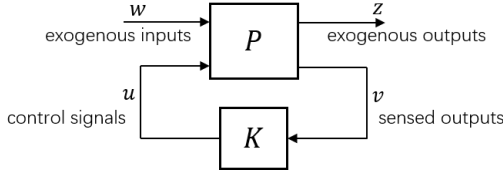


FIG. 2: Generalized H_∞ control loop.

[50], a suboptimal controller is obtained by minimizing η subject to

$$\|F_\ell(P, K)\|_\infty \leq \eta, \quad (16)$$

which reduces to a convex linear matrix inequality (LMI) feasibility problem via the Bounded Real Lemma [51].

The suboptimal H_∞ problem (16) can be solved by Mixed Sensitivity Design [52]. Its inputs are the plant G and weighting functions W_1 , W_2 , W_3 , representing performance, control effort, and robustness requirements, respectively. The synthesis ensures the frequency-dependent bounds

$$\begin{aligned} \|S\|_\infty &\leq \eta |W_1|^{-1}, \\ \|KS\|_\infty &\leq \eta |W_2|^{-1}, \\ \|T\|_\infty &\leq \eta |W_3|^{-1}. \end{aligned} \quad (17)$$

Where the sensitivity and complementary sensitivity functions are defined as $S = (I + GK)^{-1}$ and $T = GK(I + GK)^{-1}$. Enforcing an upper bound on $\|S\|$ improves low-frequency disturbance rejection and reference tracking; bounding $\|T\|$ ensures high-frequency robustness against sensor noise and unmodeled dynamics; and limiting $\|KS\|$ constrains control effort. Since H_∞ synthesis via `mixsyn` requires a state-space realization, the nonlinear DFACS dynamics, i.e., Eq. (4), Eq. (7), and Eq. (11) are linearized about the nominal drag-free trajectory. The resulting linear time-invariant (LTI) model is

$$\dot{\mathbf{x}} = \begin{bmatrix} \dot{\mathbf{p}} \\ \dot{\mathbf{p}} \end{bmatrix} = \begin{bmatrix} \mathbf{0} & \mathbf{A}_k \\ \mathbf{A}_v & \mathbf{0} \end{bmatrix} \mathbf{x} + \begin{bmatrix} \mathbf{0} \\ \mathbf{B}_v \end{bmatrix} \mathbf{u}. \quad (18)$$

The specific mathematical model is similar to that of [53], where $\mathbf{x} = [\mathbf{p}^\top \dot{\mathbf{p}}^\top]^\top$ is the state vector comprising relative position \mathbf{p} and velocity $\dot{\mathbf{p}}$. The state variables of position are defined as

$$\mathbf{p} = [\mathbf{q}_{SC} \ \mathbf{r}_{m_1 O_1}^{O_1} \ \mathbf{q}_{m_1 O_1} \ \mathbf{r}_{m_2 O_2}^{O_2} \ \mathbf{q}_{m_2 O_2}] \in \mathbb{R}^{15}, \quad (19)$$

with the inputs

$$\mathbf{u} = [\mathbf{F}_T \ \mathbf{M}_T \ \mathbf{F}_{E_1} \ \mathbf{M}_{E_1} \ \mathbf{F}_{E_2} \ \mathbf{M}_{E_2}] \in \mathbb{R}^{16}, \quad (20)$$

where $\mathbf{F}_{E_i} \in \mathbb{R}^2$ denotes the 2-D electrostatic force on the i -th TM in the plane orthogonal to its sensitive axis.

After linearization, the multiple input multiple output (MIMO) system is decoupled into 15 independent single input single output (SISO) channels via static state feedback and input allocations. Specifically, we define a desired virtual input vector $\mathbf{u}_d \in \mathbb{R}^{15}$, and compute the physical control input $\mathbf{u} \in \mathbb{R}^{16}$ as

$$\mathbf{u} = \mathbf{B}_v^\dagger (\mathbf{u}_d - \mathbf{A}_v \mathbf{p}), \quad (21)$$

where $\mathbf{B}_v^\dagger \in \mathbb{R}^{16 \times 15}$ denotes the pseudoinverse of the input matrix $\mathbf{B}_v \in \mathbb{R}^{15 \times 16}$. Substituting (21) into the velocity dynamics $\ddot{\mathbf{p}} = \mathbf{A}_v \mathbf{p} + \mathbf{B}_v \mathbf{u}$ yields the fully decoupled closed-loop form

$$\ddot{\mathbf{p}} = \mathbf{u}_d. \quad (22)$$

Provided that \mathbf{B}_v has full row rank, the original MIMO plant is transformed into 15 uncoupled integrators, one for each relative degree of freedom, which allows for independent SISO H_∞ controller design for each channel. However, since $\mathbf{B}_v \in \mathbb{R}^{15 \times 16}$ does not have a true inverse, its generalized inverse must be computed by solving the optimization problem

$$\arg \min_{\mathbf{B}_v^\dagger} \|\mathbf{I}_{15} - \mathbf{B}_v \mathbf{B}_v^\dagger\|_2. \quad (23)$$

Here, \mathbf{I}_{15} denotes the 15×15 identity matrix. Since the core task of the DFACS is to control the SC to simultaneously track the two non-orthogonal sensitive axes of the TMs, a specific control strategy for MPS is required. Denoting

$$\mathbf{r}_{m_i O_i}^{O_i} = [x_{m_i O_i}^{O_i}, y_{m_i O_i}^{O_i}, z_{m_i O_i}^{O_i}]^T.$$

To satisfy the drag-free control requirements, MPS is commanded to allocate its thrust in the SRF as follows: the x -axis thrust component generates the control force associated with the symmetric mode $x_{m_1 O_1}^{O_1} + x_{m_2 O_2}^{O_2}$, while the y -axis thrust component drives the antisymmetric mode $x_{m_1 O_1}^{O_1} - x_{m_2 O_2}^{O_2}$:

$$\begin{aligned} \mathbf{F}_{T,x} &= B_{v,1,4}^\dagger (u_{d,4} + u_{d,10}), \\ &= B_{v,1,10}^\dagger (u_{d,4} + u_{d,10}). \end{aligned} \quad (24)$$

$$\begin{aligned} \mathbf{F}_{T,y} &= B_{v,2,4}^\dagger (u_{d,4} - u_{d,10}), \\ &= B_{v,2,10}^\dagger (-u_{d,4} + u_{d,10}). \end{aligned} \quad (25)$$

Clearly, this allocation strategy imposes constraints on Eq. (23), analogous constraints for attitude channels based on the SC and TM inertia tensors (e.g., torque allocation proportional to \mathbf{J}_S^{-1} , \mathbf{J}_m^{-1}). This convex quadratic program is solved using active-set algorithm. The resulting control allocator achieves a projection error of $\|\mathbf{I}_{15} - \mathbf{B}_v \mathbf{B}_v^\dagger\|_2 = 2.2 \times 10^{-3}$, indicating near-exact command realization.

After completing the decoupling, the design of the H_∞ controller continues. Eq. (21) and Eq. (22) enable us to shift from designing a controller for \mathbf{u} to designing a controller for the decoupled SISO system \mathbf{u}_d . For each degree of freedom in \mathbf{p} , only the associated control requirements and noise characteristics pertinent to that specific degree of freedom need to be considered in determining the weighting functions in Eq. (17). The detailed DFACS control requirements are given in Table I [53]:

TABLE I: Precision requirements for drag-free and attitude control state variables.

state variable	requirement (ASD)
$x_{m_i O_i}^{O_i}$	$2.5 \times 10^{-9} \text{ m}/\sqrt{\text{Hz}}$
$y_{m_i O_i}^{O_i}, z_{m_i O_i}^{O_i}$	$5 \times 10^{-9} \text{ m}/\sqrt{\text{Hz}}$
$\varphi_{SC}, \theta_{SC}, \psi_{SC}$	$1 \times 10^{-8} \text{ rad}/\sqrt{\text{Hz}} \times \omega_b$
$\varphi_{m_i O_i}$	$2 \times 10^{-7} \text{ rad}/\sqrt{\text{Hz}} \times \omega_b$
$\theta_{m_i O_i}, \psi_{m_i O_i}$	$1 \times 10^{-8} \text{ rad}/\sqrt{\text{Hz}} \times \omega_b$

Based on these requirements, the weighting functions W_1 and W_3 corresponding to each degree of freedom can be calculated as

$$W_1 = \frac{PF_u}{B}, \quad (26)$$

$$W_3 = \frac{PF_y}{B}. \quad (27)$$

Where F_u is the transfer function determined by the exogenous disturbance model, F_y is the transfer function determined by the measurement noise model, and B is determined by the control requirements of each state variable. In the disturbance models, special attention is given to solar radiation pressure (SRP), with its transfer function given by [54]

$$\mathbf{F}_{SRP} = (k_{dSC} + H_{press} w) \mathbf{T}_I^S \frac{\mathbf{r}_{SI}^I}{\|\mathbf{r}_{SI}^I\|_2}. \quad (28)$$

The corresponding torque is

$$\mathbf{D}_{SRP} = \begin{bmatrix} 0 & -0.6 & 0 \\ 0.6 & 0 & -0.1 \\ 0 & 0.1 & 0 \end{bmatrix} \mathbf{F}_{SRP}. \quad (29)$$

The constant k_{dSC} is derived from the solar radiation pressure constant at the SC's orbital distance and the effective area of its solar arrays [55]. Given the similarity in

orbital configuration ($\mathbf{r}_{SI}^I \approx 1 \text{ AU}$) and spacecraft structural layout, we adopt the value used in the LISA mission studies, namely, $k_{dSC} = 6.3513 \times 10^{-5} \text{ N}$, which is significantly larger than the magnitude of the transfer function H_{press} ($\sim 1 \times 10^{-10} \text{ N}$). Therefore, including SRP directly in F_u would significantly increase the requirements on W_1 in the low-frequency range, making Eq. (17) difficult to solve. To address this issue, we introduce a feedforward channel that leverages spacecraft orbit determination data to estimate $\hat{\mathbf{r}}_{SI}^I$. Based on Taiji's exceptional orbital stability and its periodic ground-based orbit determination architecture, a conservative 50-km 1σ position estimation error is assumed for $\hat{\mathbf{r}}_{SI}^I$ [56]. This allows for the estimation of the ultra-low-frequency components of \mathbf{F}_{SRP} and \mathbf{D}_{SRP} , denoted as $\hat{\mathbf{F}}_{SRP,C}$ and $\hat{\mathbf{D}}_{SRP,C}$

$$\hat{\mathbf{F}}_{SRP,C} = k_{dSC} \mathbf{T}_I^S \frac{\hat{\mathbf{r}}_{SI}^I}{\|\hat{\mathbf{r}}_{SI}^I\|_2}, \quad (30)$$

$$\hat{\mathbf{D}}_{SRP,C} = \begin{bmatrix} 0 & -0.6 & 0 \\ 0.6 & 0 & -0.1 \\ 0 & 0.1 & 0 \end{bmatrix} \hat{\mathbf{F}}_{SRP}. \quad (31)$$

Thus, the SRP contribution to the state acceleration $\ddot{\mathbf{p}}$ is compensated by

$$\hat{\mathbf{a}}_{SRP} = \begin{bmatrix} \mathbf{J}_S^{-1} \hat{\mathbf{D}}_{SRP,C} \\ m_S^{-1} \mathbf{T}_S^{O_1} \hat{\mathbf{F}}_{SRP} \\ \mathbf{0}_{3 \times 1} \\ m_S^{-1} \mathbf{T}_S^{O_2} \hat{\mathbf{F}}_{SRP} \\ \mathbf{0}_{3 \times 1} \end{bmatrix}. \quad (32)$$

This allows Eq. (21) to be rewritten as

$$\mathbf{u} = \mathbf{B}_v^\dagger (\mathbf{u}_d - \mathbf{A}_V \hat{\mathbf{p}} - \hat{\mathbf{a}}_{SRP}), \quad (33)$$

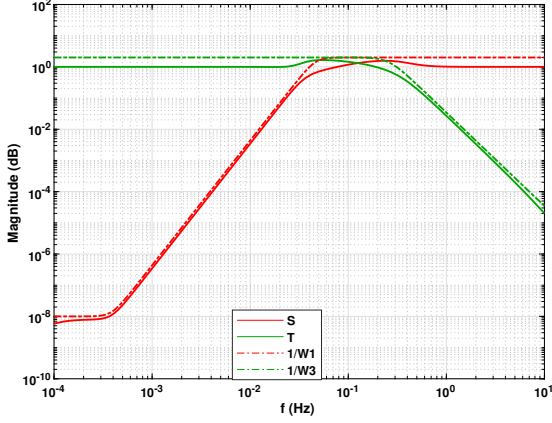
thereby preventing k_{dSC} from being introduced into F_u .

Figure 3 shows the mixed-sensitivity H_∞ controller design results. Critically, both the sensitivity function S and the complementary sensitivity function T satisfy their respective performance bounds over the entire bandwidth, confirming the feasibility of the robust specification.

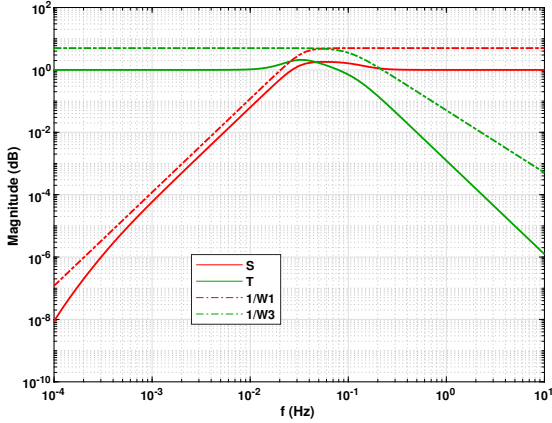
B. Simulation result

Following the completion of the controller synthesis, a high-fidelity Simulink-based DFACS simulation was developed for closed-loop validation, with the architecture and data flow shown in Figure 4.

The simulation runs at 10 Hz over 25 days, initialized at 2035-01-01T00:00:00 UTC using DE440. Initial state perturbations of \mathbf{p} are zero-mean Gaussian with $\sigma = 5 \times 10^{-8} \text{ m}$ for position variables and $5 \times 10^{-8} \text{ rad}$ for attitude variables. The system incorporates actuation noises, environmental noises, and sensor readout noises, all based on the noise models published by [57, 58].



(a) Results for the sensitive axis $x_{m_1 O_1}^{O_1}$ (primary performance channel), showing S , T , and their bounds W_1^{-1} , W_3^{-1} .



(b) Corresponding S and T responses for the transverse axes $y_{m_1 O_1}^{O_1}$ and $z_{m_1 O_1}^{O_1}$.

FIG. 3: Design verification of the H_∞ controller: sensitivity (S) and complementary sensitivity (T) functions versus frequency. All curves remain within their prescribed bounds, demonstrating robust performance.

The DFACS simulation outputs both the true state \mathbf{p} and its sensor readout $\hat{\mathbf{p}}$. To assess compliance with the requirements in Table I, the amplitude spectral densities (ASDs) of $\mathbf{r}_{m_1 O_1}^{O_1}$, $\mathbf{r}_{m_2 O_2}^{O_2}$, and \mathbf{q}_{SC} are plotted in Figure 5. The above simulation results demonstrate that, within the measurement frequency band of 0.1 mHz to 1 Hz, the DFACS achieves the control requirements for each degree of freedom of \mathbf{p} as specified in Table I. Compared to the latest reported control performance of LISA [49], these results show superior performance in the low-frequency band, which is attributed to the feedforward control design for the constant component of SRP.

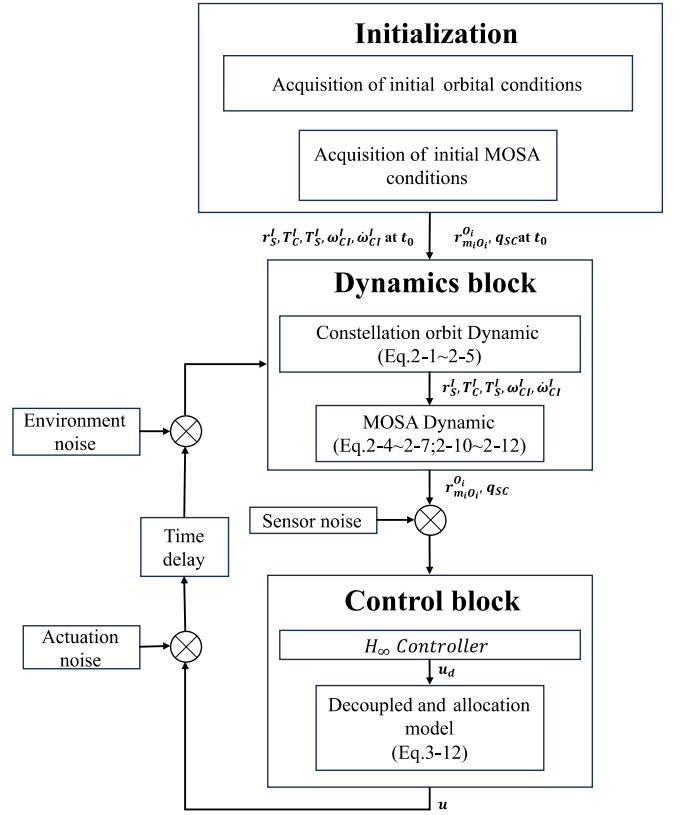


FIG. 4: Flow chart for the DFACS simulation.

IV. COM OFFSET CALIBRATION PRINCIPLE AND RESULTS

A. Principle of CoM Offset Calibration in Science Mode

We further discuss the relationship between the acceleration $\ddot{\mathbf{r}}_{m_i O_i}^{O_i}$ and the coupling acceleration

$$\mathbf{a}_{\dot{\omega},i} := -\boldsymbol{\Omega}(\omega_{SI}^S) \mathbf{T}_S^I \mathbf{b}_i^S$$

induced by the SC attitude jitter. Based on the simulation results, the amplitude spectral density of the acceleration data $\ddot{\mathbf{r}}_{m_1 O_1}^{O_1}$ and $\mathbf{a}_{\dot{\omega},1}$ is shown in Figures 6. In the maneuver-based calibration scheme, high-amplitude square-wave angular maneuvers render the angular acceleration-induced inertial term $\mathbf{a}_{\dot{\omega},i}$ the dominant contribution to the TM relative acceleration $\ddot{\mathbf{r}}_{m_i O_i}^{O_i}$, producing a spectrally isolated peak at the maneuver frequency. Consequently, the readout $\ddot{\mathbf{r}}_{m_1 O_1}^{O_1}$ can be modeled as,

$$\ddot{\mathbf{r}}_{m_i O_i}^{O_i} = \mathbf{a}_{\dot{\omega},i} + \mathbf{a}_{wn}, \quad (34)$$

where \mathbf{a}_{wn} denotes additive Gaussian white noise.

In contrast, during science mode calibration (i.e., without dedicated maneuvers), $\mathbf{a}_{\dot{\omega},i}$ is neither dominant nor spectrally isolated, as evidenced by the broadband spectra in Figs. 6. Instead, Substituting Eq. (3) into Eq. (4)

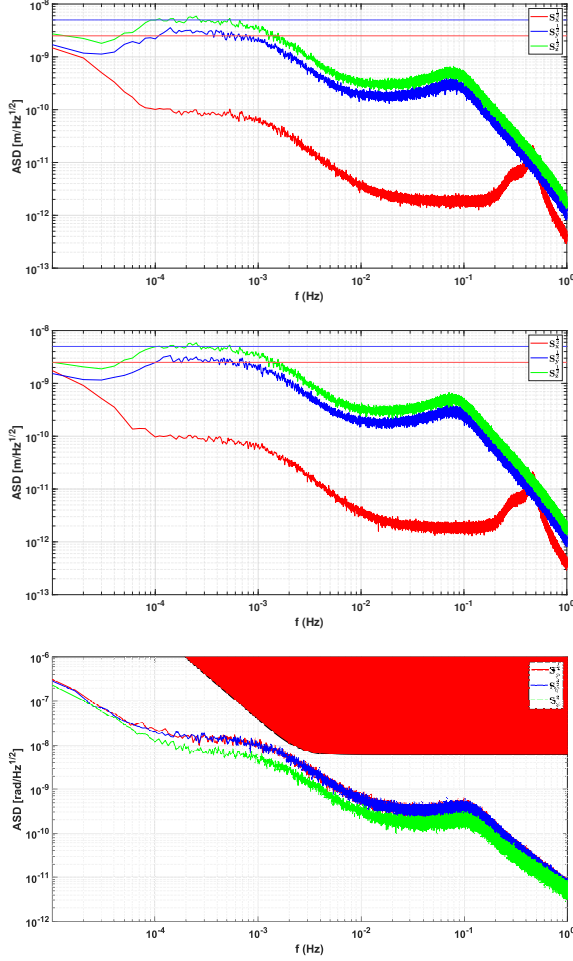


FIG. 5: Simulation results of $\mathbf{r}_{m_i O_i}^O$ and \mathbf{q}_{SC} (converted to Euler angles). Control requirements are overlaid for reference: in the $\mathbf{r}_{m_i O_i}^O$ subplot, the red solid line denotes the requirement along the sensitive axis, while the blue solid lines correspond to the non-sensitive axes.

yields:

$$\begin{aligned} \ddot{\mathbf{r}}_{m_i O_i}^O &= \mathbf{T}_I^O \left[\Delta \mathbf{a}_{g,i} + m_M^{-1} \mathbf{T}_O^I (\mathbf{F}_E + \mathbf{F}_{st} + \mathbf{d}_M) \right. \\ &\quad \left. - m_S^{-1} \mathbf{T}_S^I (\mathbf{F}_T + \mathbf{d}_S - \sum_{j=1}^2 \mathbf{T}_{O_j}^S \mathbf{F}_{E_j}) \right. \\ &\quad \left. + \mathbf{T}_S^I \mathbf{a}_{\dot{\omega},i} \right], \end{aligned} \quad (35)$$

where $\Delta \mathbf{a}_{g,i} = \mathbf{a}_g(\mathbf{r}_{m_i I}^I) - \mathbf{a}_g(\mathbf{r}_{SC I}^I) + \mathbf{T}_O^I \mathbf{a}_{sg,i}$ denotes the differential gravitational acceleration between the SC and the i -th TM, with $\mathbf{a}_{sg,i}$ representing the self-gravitational bias. To account for the full dynamics of Eq. (35), we

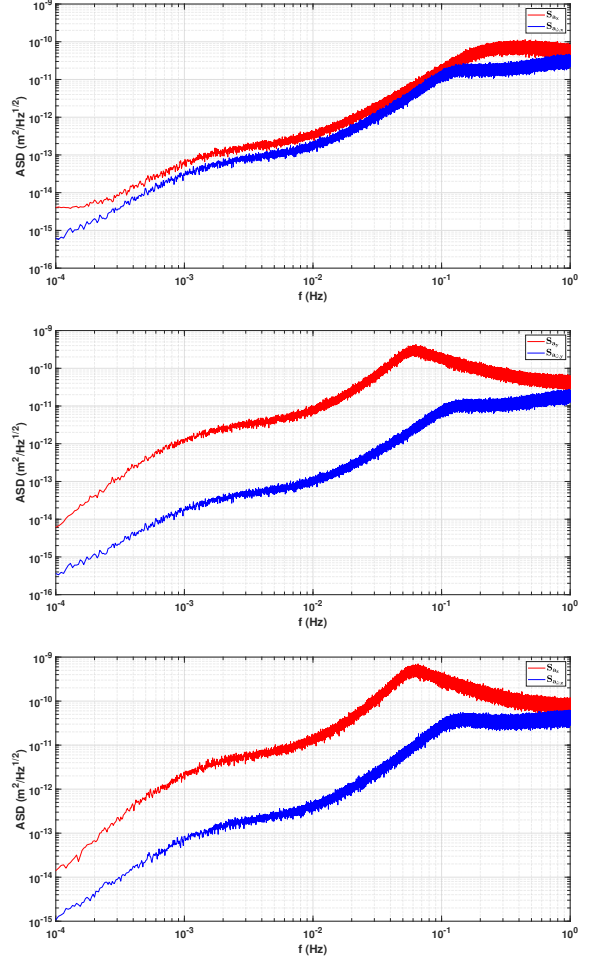


FIG. 6: The amplitude spectral density plot of $\ddot{\mathbf{r}}_{m_1 O_1}^{O1}$ and $\mathbf{a}_{\dot{\omega},1}$, from left to right, corresponds to the x, y, and z-axis data, with the red line representing $\ddot{\mathbf{r}}_{m_1 O_1}^{O1}$ and the blue line representing $\mathbf{a}_{\dot{\omega},1}$.

propose an extended state space representation:

$$\dot{\mathbf{X}}_i \equiv \begin{bmatrix} \dot{\mathbf{r}}_{m_i O_i}^O \\ \ddot{\mathbf{r}}_{m_i O_i}^O \\ \dot{\mathbf{a}}_{b,i}^O \\ \dot{\mathbf{b}}_i^O \\ \dot{\mathbf{n}}_i \end{bmatrix} = \mathbf{A}_i \begin{bmatrix} \mathbf{r}_{m_i O_i}^O \\ \dot{\mathbf{r}}_{m_i O_i}^O \\ \mathbf{a}_{b,i}^O \\ \mathbf{b}_i^O \\ \mathbf{n}_i \end{bmatrix} + \mathbf{B} \begin{bmatrix} \mathbf{u}_i \\ \mathbf{u}_{n,i} \end{bmatrix}, \quad (36)$$

with the associated readout model

$$\mathbf{r}_{m_i O_i}^O = \mathbf{H} \begin{bmatrix} \mathbf{r}_{m_i O_i}^O \\ \dot{\mathbf{r}}_{m_i O_i}^O \\ \mathbf{a}_{b,i}^O \\ \mathbf{b}_i^O \\ \mathbf{n}_i \end{bmatrix} + \mathbf{D}_{n,i} \mathbf{u}_{n,i}. \quad (37)$$

In Eq. (36), the state vector comprises the relative displacement $\mathbf{r}_{m_i O_i}^O$, the bias acceleration $\mathbf{a}_{b,i}^O$, the SC-TM COM offset expressed in ORF $_i$, $\mathbf{b}_i^O = \mathbf{T}_S^O \mathbf{b}_i^S$, and the

state variables of the measurement noise shape, \mathbf{n}_i . The residual measurement noise is modeled as additive Gaussian white noise $\mathbf{u}_{n,i}$. The extended state-space matrices \mathbf{A}_i , \mathbf{B} , and \mathbf{H} are defined as

$$\mathbf{A}_{i,22 \times 22} = \begin{bmatrix} \begin{bmatrix} \mathbf{0}_{3 \times 3} & \mathbf{I}_{3 \times 3} & \mathbf{0}_{3 \times 6} \\ \mathbf{0}_{3 \times 6} & \mathbf{I}_{3 \times 3} & \boldsymbol{\Omega}_{i,3 \times 3} \\ \mathbf{0}_{6 \times 12} & & \mathbf{0}_{6 \times 6} \end{bmatrix} & \mathbf{0}_{12 \times 10} \\ & \mathbf{A}_{n,10 \times 10} \end{bmatrix},$$

$$\mathbf{B}_{22 \times 6} = \begin{bmatrix} \begin{bmatrix} \mathbf{0}_{3 \times 3} \\ \mathbf{I}_{3 \times 3} \\ \mathbf{0}_{6 \times 3} \\ \mathbf{0}_{12 \times 3} \end{bmatrix} & \mathbf{0}_{10 \times 3} \\ & \mathbf{B}_{n,10 \times 3} \end{bmatrix},$$

$$\mathbf{H}_{3 \times 22} = [\mathbf{I}_{3 \times 3} \quad \mathbf{0}_{3 \times 9} \quad \mathbf{C}_{n,3 \times 10}],$$

$$\boldsymbol{\Omega}_{i,3 \times 3} = [\mathbf{T}_S^{O_i} \dot{\omega}_{\text{SI}}]^\times.$$

For readability, the subscript i used to distinguish TM1 and TM2 is omitted when referring to the parameters \mathbf{A}_i in the subsequent text.

The inputs \mathbf{u}_i , including control forces, torques, as well as the noise forces and torques, are estimated as

$$\hat{\mathbf{u}}_i = \begin{bmatrix} m_M^{-1} \mathbf{T}_O^I (\hat{\mathbf{F}}_E + \hat{\mathbf{F}}_{\text{st}}) - m_S^{-1} \mathbf{T}_S^I (\hat{\mathbf{F}}_T + \hat{\mathbf{F}}_{\text{SRP},C} - \sum_{i=1}^2 \mathbf{T}_{O_i}^S \hat{\mathbf{F}}_{E_i}) \\ \hat{\mathbf{M}}_T + \hat{\mathbf{D}}_{\text{SRP},C} - \sum_{i=1}^2 \mathbf{T}_{O_i}^S \hat{\mathbf{M}}_{E_i} \end{bmatrix}.$$

In Eq. (36), \mathbf{n}_i denotes the state vector of the shaped readout noise process. Since the Taiji mission has not yet released a comprehensive, publicly available characterization of its sensor noise transfer functions, we adopt the experimentally validated noise models from the LISA mission [57]. This choice is justified by the high similarity between Taiji and LISA in scientific objectives, orbital environment, and core sensor technologies. Based on these established transfer-function models for the IS, IFO, and DWS, the corresponding state-space realizations for \mathbf{n}_i can be constructed as

$$\begin{aligned} \dot{\mathbf{n}} &= \mathbf{A}_n \mathbf{n} + \mathbf{B}_n \mathbf{u}_n, \\ \mathbf{y}_n &= \mathbf{C}_n \mathbf{n} + \mathbf{D}_n \mathbf{u}_n. \end{aligned}$$

With the extended state-space model Eqs.(36)–(37) established, the CoM offset $\mathbf{b}_i^{O_i}$ and other latent states can be jointly estimated from the DFACS readout $\tilde{\mathbf{r}}_{m_i, O_i}^{O_i}$ through Kalman filtering methods. In the following, we introduce an adaptive Kalman filter algorithm that recursively updates the state estimates and covariance matrices, enabling robust calibration of $\mathbf{b}_i^{O_i}$ in the presence of model uncertainties and time-varying disturbances.

B. Addaptive Kalman filter

In previous work for maneuver-based COM offset calibration, algorithms such as least squares estimation or Kalman filtering [59] have typically been used to estimate the CoM offset [34, 37, 38]. This paper continues this approach by using Kalman filtering for calibration. Based

on Eq. (36), the following Kalman filter is constructed:

$$\hat{\mathbf{X}}_{k+1}^- = \mathbf{A}_d \hat{\mathbf{X}}_k^+ + \mathbf{B}_d \begin{bmatrix} \mathbf{u}_i \\ \mathbf{u}_{n,i} \end{bmatrix}, \quad (38)$$

$$\mathbf{d}_k = \tilde{\mathbf{r}}_{m_i, O_i}^{O_i} - \mathbf{H} \hat{\mathbf{X}}_{k+1}^-, \quad (39)$$

$$\mathbf{K}_k = \mathbf{P}_k \mathbf{H}^\top (\mathbf{H} \mathbf{P}_k \mathbf{H}^\top + \mathbf{R}_k)^{-1}, \quad (40)$$

$$\hat{\mathbf{X}}_{k+1}^+ = \hat{\mathbf{X}}_{k+1}^- + \mathbf{K}_k \mathbf{d}_k, \quad (41)$$

$$\mathbf{P}_{k+1} = \mathbf{A}_d (\mathbf{I} - \mathbf{K}_k \mathbf{H}) \mathbf{P}_k \mathbf{A}_d^\top + \mathbf{Q}_k. \quad (42)$$

In these equations, \mathbf{A}_d and \mathbf{B}_d are the discrete forms of \mathbf{A} and \mathbf{B} in Eq. (36). The subscript k denotes the discrete time index corresponding to the k -th measurement update. The Kalman gain is denoted by \mathbf{K}_k , and \mathbf{d}_k is the innovation vector. The state error covariance matrix is $\mathbf{P}_k = \mathbb{E}\{\boldsymbol{\delta} \mathbf{X}_k \boldsymbol{\delta} \mathbf{X}_k^\top\}$, where $\boldsymbol{\delta} \mathbf{X}_k = \mathbf{X}_k - \hat{\mathbf{X}}_k$ represents the state error vector, defined as the difference between the true state and the estimated state at time step k . The measurement noise covariance matrix is $\mathbf{R}_k = \mathbb{E}\{\mathbf{v}_k \mathbf{v}_k^\top\}$, and the process noise covariance matrix is $\mathbf{Q}_k = \mathbb{E}\{\mathbf{w}_k \mathbf{w}_k^\top\}$.

In a standard Kalman filter, \mathbf{Q}_k and \mathbf{R}_k are given as constant matrices. Thus, for the high-dimensional extended state vector $\mathbf{X}_{i,22 \times 1}$, the filter requires specifying $\hat{\mathbf{Q}}_{i,22 \times 22}$ and $\hat{\mathbf{R}}_{i,3 \times 3}$. However, the performance of the Kalman filter is highly sensitive to \mathbf{Q} and \mathbf{R} [60, 61]. Let

the matrix elements of $\mathbf{Q}_{n \times n}$ be $q_{i,j}$ and those of $\mathbf{R}_{p \times p}$ be $r_{i,j}$, and define γ :

$$\gamma = q_{1,1} : q_{1,2} : \cdots : q_{n,n} : r_{1,1} : r_{1,2} : \cdots : r_{p,p}$$

where γ represents the model parameter ratio of \mathbf{Q} and \mathbf{R} . Given estimates $\hat{\mathbf{Q}}$ and $\hat{\mathbf{R}}$, the filter is optimal if and only if $\hat{\gamma} = \gamma$. For the present extended state model, γ is 493-dimensional, making direct iterative tuning of $\hat{\mathbf{Q}}$ and $\hat{\mathbf{R}}$ impractical. To address this, we employ an adaptive Kalman filter based on the Sage-Husa method [62, 63], which falls within the class of covariance matching techniques, a well-established approach for the estimation of process and measurement noise covariances [64, 65].

$$\mathbf{Q}_k = \mathbf{P}_{k+1} - \mathbf{A}_d \mathbf{P}_k \mathbf{A}_d^\top + \mathbf{K}_k \mathbf{S}_k \mathbf{K}_k^\top, \quad (43)$$

where $\mathbf{S}_k = \mathbb{E}\{\mathbf{d}_k \mathbf{d}_k^\top\}$ is the innovation covariance. Using exponential weighting, the iterative estimate of \mathbf{Q}_k is given by

$$\hat{\mathbf{Q}}_k = \alpha \hat{\mathbf{Q}}_{k-1} + (1-\alpha) [\mathbf{P}_{k+1} - \mathbf{A}_d \mathbf{P}_k \mathbf{A}_d^\top + \mathbf{K}_k \mathbf{S}_k \mathbf{K}_k^\top], \quad (44)$$

and similarly for \mathbf{R}_k :

$$\hat{\mathbf{R}}_k = \alpha \hat{\mathbf{R}}_{k-1} + (1-\alpha) [\mathbf{S}_k - \mathbf{H} \mathbf{P}_k \mathbf{H}^\top], \quad (45)$$

where $\alpha \in (0, 1)$ is the adaptation gain. The updating procedure in Eqs. (44)–(45) constitutes the innovation-based covariance matching method. However, this approach does not guarantee the positive definiteness of $\hat{\mathbf{Q}}_k$ and $\hat{\mathbf{R}}_k$, which may lead to filter divergence in high-dimensional settings. To enforce positive definiteness, the residual-based covariance matching method is often adopted [66]:

$$\hat{\mathbf{Q}}_k = \alpha \hat{\mathbf{Q}}_{k-1} + (1-\alpha) \mathbf{K}_k \mathbf{S}_k \mathbf{K}_k^\top, \quad (46)$$

$$\hat{\mathbf{R}}_k = \alpha \hat{\mathbf{R}}_{k-1} + (1-\alpha) [\mathbb{E}\{\boldsymbol{\varepsilon}_k \boldsymbol{\varepsilon}_k^\top\} + \mathbf{H} \mathbf{P}_k \mathbf{H}^\top], \quad (47)$$

where the residual $\boldsymbol{\varepsilon}_k$ is defined as

$$\boldsymbol{\varepsilon}_k = \tilde{\mathbf{r}}_{m_i O_i}^{O_i} - \mathbf{H} \hat{\mathbf{X}}_{k+1}^+. \quad (48)$$

This formulation ensures positive definite covariance estimates and thus stable filtering. Nevertheless, by replacing $\mathbf{P}_{k+1} - \mathbf{A}_d \mathbf{P}_k \mathbf{A}_d^\top$ with zero in Eq. (46), the residual-based method relaxes the statistical consistency between $\hat{\mathbf{Q}}_k$ and the true process noise, potentially degrading estimation accuracy for complex, high-dimensional systems.

Conventional covariance matching approaches are subject to two fundamental limitations: the innovation-based formulation does not guarantee the positive definiteness of the updated covariance, while the residual-based variant produces statistically inconsistent state estimates. To ensure the stability and convergence of the filter, we employ a monotonic-update scheme throughout the estimation process.

Let $|\cdot|$ denote the element-wise absolute value of a matrix, and let $\min\{\cdot, \cdot\}$ represent the element-wise minimum operator. The update equations are then given by

$$\hat{\mathbf{R}}_{\text{iter}} = \hat{\mathbf{S}}_k - \mathbf{H} \mathbf{P}_k \mathbf{H}^\top, \quad (49)$$

$$\hat{\mathbf{R}}_k = \alpha \hat{\mathbf{R}}_{k-1} + (1-\alpha) \min\{|\hat{\mathbf{R}}_{\text{iter}}|, \hat{\mathbf{R}}_{k-1}\}, \quad (50)$$

$$\hat{\mathbf{Q}}_{\text{iter}} = \hat{\mathbf{P}}_{k+1} - \mathbf{A}_d \mathbf{P}_k \mathbf{A}_d^\top + \mathbf{K}_k \hat{\mathbf{S}}_k \mathbf{K}_k^\top, \quad (51)$$

$$\hat{\mathbf{Q}}_k = \alpha \hat{\mathbf{Q}}_{k-1} + (1-\alpha) \min\{|\hat{\mathbf{Q}}_{\text{iter}}|, \hat{\mathbf{Q}}_{k-1}\}. \quad (52)$$

However, the enforced monotonicity may prevent convergence when initial estimates are overly conservative.

To resolve this, we retain the monotonic update for $\hat{\mathbf{Q}}_k$ (critical for process-noise stability) but relax it for $\hat{\mathbf{R}}_k$, exploiting the availability of reliable a priori sensor noise characterization. The forgetting factor $(1-\alpha)$ is thus shifted to the innovation residual computation:

$$\hat{\mathbf{R}}_{\text{iter}} = (1-\alpha) (\hat{\mathbf{S}}_k - \mathbf{H} \mathbf{P}_k \mathbf{H}^\top) \quad (53)$$

$$\hat{\mathbf{R}}_k = \alpha \hat{\mathbf{R}}_{k-1} + \min\{|\hat{\mathbf{R}}_{\text{iter}}|, \hat{\mathbf{R}}_{k-1}\} \quad (54)$$

The $\hat{\mathbf{Q}}_k$ update remains as in Eqs. (51)–(52). We refer to this enhanced scheme as the proposed adaptive covariance matching method used in the COM offset calibration.

Finally, the Extended-State Kalman Filter is equipped with the proposed adaptive covariance matching algorithm, yielding the Extended-State Adaptive Kalman Filter (ES-AKF) formulated as follows:

$$\hat{\mathbf{X}}_{k+1}^- = \mathbf{A}_d \hat{\mathbf{X}}_k^+ + \mathbf{B}_d \begin{bmatrix} \mathbf{u}_i \\ \mathbf{u}_{n,i} \end{bmatrix}, \quad (55)$$

$$\mathbf{d}_k = \tilde{\mathbf{r}}_{m_i O_i}^{O_i} - \mathbf{H} \hat{\mathbf{X}}_{k+1}^-, \quad (56)$$

$$\hat{\mathbf{R}}_{\text{iter}} = (1-\alpha) (\hat{\mathbf{S}}_k - \mathbf{H} \mathbf{P}_k \mathbf{H}^\top), \quad (57)$$

$$\hat{\mathbf{R}}_k = \alpha \hat{\mathbf{R}}_{k-1} + \min\{|\hat{\mathbf{R}}_{\text{iter}}|, \hat{\mathbf{R}}_{k-1}\}, \quad (58)$$

$$\mathbf{K}_k = \mathbf{P}_k \mathbf{H}^\top (\mathbf{H} \mathbf{P}_k \mathbf{H}^\top + \mathbf{R}_k)^{-1}, \quad (59)$$

$$\hat{\mathbf{X}}_{k+1}^+ = \hat{\mathbf{X}}_{k+1}^- + \mathbf{K}_k \mathbf{d}_k, \quad (60)$$

$$\hat{\mathbf{Q}}_{\text{iter}} = \hat{\mathbf{P}}_{k+1} - \mathbf{A}_d \mathbf{P}_k \mathbf{A}_d^\top + \mathbf{K}_k \hat{\mathbf{S}}_k \mathbf{K}_k^\top, \quad (61)$$

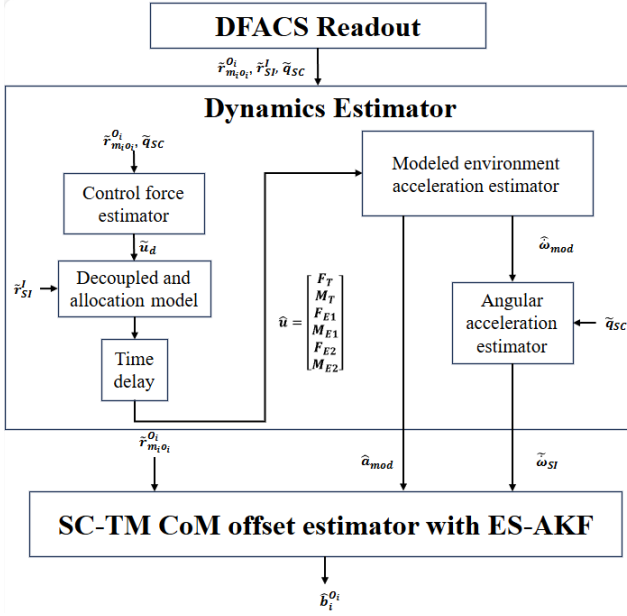


FIG. 7: Procedure of CoM offset calibration.

$$\hat{\mathbf{Q}}_k = \alpha \hat{\mathbf{Q}}_{k-1} + (1 - \alpha) \min \left\{ |\hat{\mathbf{Q}}_{iter}|, \hat{\mathbf{Q}}_{k-1} \right\}, \quad (62)$$

$$\mathbf{P}_{k+1} = \mathbf{A}_d (\mathbf{I} - \mathbf{K}_k \mathbf{H}) \mathbf{P}_k \mathbf{A}_d^T + \mathbf{Q}_k. \quad (63)$$

Figure 7 summarizes the CoM offset calibration procedure by ES-AKF based on Eqs.(55)-(63). For comparison, its performance is evaluated against the innovation-based and residual-based methods on the TM1-SC relative displacement readout $\tilde{\mathbf{r}}_{m_1 O_1}^{O_1}$. Figures 8–10 compare the filtering performance of three adaptive Kalman filter variants: the innovation-based method, the residual-based method, and the proposed approach. These are evaluated on the TM1-SC relative displacement $\mathbf{r}_{m_1 O_1}^{O_1}$ along its three axes. The plots show the true trajectory (red), the raw readout data (yellow), the innovation-based estimate (blue), the residual-based estimate (green), and the proposed estimate (black).

Along all three axes, the innovation-based AKF (blue) exhibits severe noise amplification due to instability arising from non-positive-definite covariance updates. This is most evident for the x -axis, where the filter generates high-amplitude spikes that exceed the measurement range. The residual-based AKF (green) avoids such instabilities but introduces a noticeable phase lag relative to the true signal, particularly in regions of rapid motion. In contrast, the proposed AKF (black) achieves near-perfect tracking of the true trajectory across all axes. It suppresses measurement noise without introducing phase distortion or amplitude bias, thereby delivering higher fidelity and precise temporal alignment with the ground truth.

Therefore, in light of its superior noise suppression, phase fidelity, and robust convergence, we will adopt the proposed AKF for CoM offset calibration.

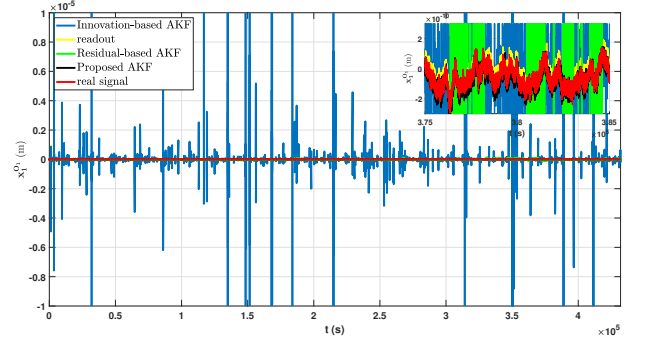


FIG. 8: Adaptive Kalman filter results of $\tilde{x}_{m_1 O_1}^{O_1}$.

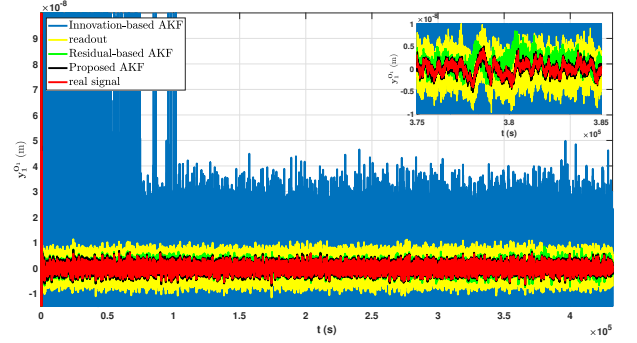


FIG. 9: Adaptive Kalman filter results of $\tilde{y}_{m_1 O_1}^{O_1}$.

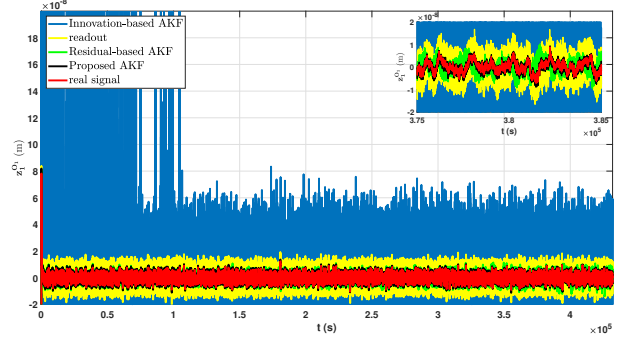


FIG. 10: Adaptive Kalman filter results of $\tilde{z}_{m_1 O_1}^{O_1}$.

C. Simulation Result

Using the science mode readouts, the ES-AKF estimates the CoM offsets $\mathbf{b}_1^{O_1}$ and $\mathbf{b}_2^{O_2}$ of TM1 and TM2 relative to the spacecraft. The convergence behavior of these estimates is presented in Figures 11 and 12.

Figures 11 and 12 show that the estimates of $\mathbf{b}_{i,x}^{O_i}$ exhibit slower convergence compared to those of $\mathbf{b}_{i,y}^{O_i}$ and $\mathbf{b}_{i,z}^{O_i}$. This behavior arises because the x -axis CoM calibration relies solely on IS readout signals ($\tilde{y}_{m_i O_i}^{O_i}$, $\tilde{z}_{m_i O_i}^{O_i}$), which have lower precision, whereas the y - and z -axis calibrations additionally utilize the high-precision IFO readout ($\tilde{x}_{m_i O_i}^{O_i}$). Consequently, $\mathbf{b}_{i,y}^{O_i}$ and $\mathbf{b}_{i,z}^{O_i}$ converge

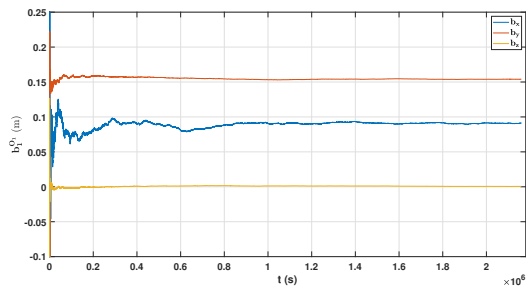


FIG. 11: The CoM offset calibration result $\mathbf{b}_1^{O_1}$.

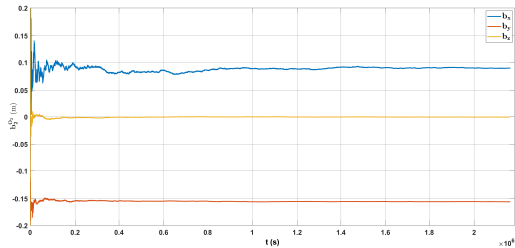


FIG. 12: The CoM offset calibration result $\mathbf{b}_2^{O_2}$.

using data of approximately 0.4×10^6 s in duration, while the $\mathbf{b}_{i,x}^{O_i}$ requires approximately 1.4 to 1.6×10^6 s. Correspondingly, when evaluated using the confidence level determined from the error covariance matrix, the final calibration accuracy of $\mathbf{b}_{1,x}^{O_1}$ is lower than that of $\mathbf{b}_{1,y}^{O_1}$ and $\mathbf{b}_{1,z}^{O_1}$. Table II lists the calibrated values, the true values, and the confidence levels computed from the final state error covariance matrix \mathbf{P}_{end} (taken as \mathbf{P}_{∞}) at the termination time.

Based on the results in Table II, the system identification algorithm using the ES-AKF estimator achieves high-precision calibration of the SC-TM CoM offset in science mode using only IS/IFO/DWS readout signals. The confidence levels are better than 4 mm for $\mathbf{b}_{i,x}^{O_i}$, better than 0.2 mm for $\mathbf{b}_{i,y}^{O_i}$, and better than 0.1 mm for $\mathbf{b}_{i,z}^{O_i}$. However, the calibrated value of $\mathbf{b}_{i,x}^{O_i}$ is actually closer to the true value than that of $\mathbf{b}_{i,y}^{O_i}$. This phenomenon can be explained by two factors.

First, the calibration value is determined as the mathematical expectation of all estimates over the final 3600 s of data. In theory, the estimate of $\mathbf{b}_i^{O_i}$ oscillates around or slowly approaches the true value. Therefore, the close agreement between the $\mathbf{b}_{i,x}^{O_i}$ estimate and the true value indicates that its convergence point is near the true value. Nevertheless, its error variance—i.e., the amplitude of oscillation—remains the largest among the three degrees of freedom. This behavior is clearly illustrated by the

convergence curves in Figures 11 and 12.

Second, the relative displacement $\mathbf{r}_{m_i O_i}^{O_i}$ exhibits higher noise in the ultra-low-frequency band below the control bandwidth along the sensitive axis (as shown in Figure 5), which does not affect control requirements but significantly impacts the estimation accuracy of $\mathbf{x}_{m_i O_i}^{O_i}$ by the AKF in the ultra-low-frequency range (see Figure 8), thereby affecting the estimation of $\mathbf{b}_{i,y}^{O_i}$.

Overall, comparing the true values with the estimated results, the estimation errors of the SC-TM CoM offset using the ES-AKF estimator—based solely on scientific data readout—are less than 1%.

V. CONCLUSION

This work proposes and validates a maneuver-free calibration scheme for the SC-TM CoM offset during the science operation of space-based gravitational-wave antennas, especially for Taiji (a typical LISA-like mission). The method directly utilizes the standard science-mode readouts of the IS, interferometer, and differential wavefront sensor, eliminating the need for dedicated spacecraft maneuvers that disrupt measurement continuity and laser-link stability.

A high-fidelity, closed-loop simulation framework was developed, integrating a detailed nonlinear dynamics model of the LISA-like SC-TM system and a robust H_{∞} drag-free and attitude controller. Using 25 days of simulated science data, we designed an Extended-State Adaptive Kalman Filter that incorporates the CoM offset induced acceleration noises, sensor noise dynamics, and systematic biases into a unified state-estimation framework. The filter successfully identifies the CoM offset vector with an accuracy of 0.01–1.5 mm across all axes, corresponding to a maximum relative error below 1%.

Beyond calibration, the proposed ES-AKF demonstrates the capability of high-precision filtering of the IS readout signal and suppression of noise. Under the condition that the IS noise is accurately modeled, the filter suppresses the IS readout noise from 1×10^{-9} m/ $\sqrt{\text{Hz}}$ to 1×10^{-11} m/ $\sqrt{\text{Hz}}$. This result suggests that the ES-AKF can be integrated or embedded into the DFACS to enhance measurement quality and significantly improve control performance.

In summary, this study provides a viable and precise calibration strategy that can operate continuously during science observations, enabling the largest nonlinear disturbance in the DFACS to be accurately predicted. The framework also contributes a model-based estimation tool that supports advanced DFACS functions including disturbance compensation, performance diagnostics, and nonlinear control design.

[1] M. Colpi, K. Danzmann, M. Hewitson, K. Holley-Bockelmann, P. Jetzer, G. Nelemans, A. Petiteau,

D. Shoemaker, C. Sopena, R. Stebbins, *et al.*, Lisa

TABLE II: SC-TM CoM Offset Calibration Results

State variable	Calibration Value (Unit: m)	Uncertainty (Unit: m)	True Value (Unit: m)
$\mathbf{b}_{1,x}^0$	9.081×10^{-2}	1.335×10^{-3}	9.087×10^{-2}
$\mathbf{b}_{1,y}^0$	1.540×10^{-1}	1.705×10^{-4}	1.554×10^{-1}
$\mathbf{b}_{1,z}^0$	5.086×10^{-4}	9.219×10^{-5}	0
$\mathbf{b}_{2,x}^0$	9.019×10^{-2}	3.762×10^{-3}	9.087×10^{-2}
$\mathbf{b}_{2,y}^0$	-1.553×10^{-1}	1.394×10^{-4}	-1.554×10^{-1}
$\mathbf{b}_{2,z}^0$	-3.509×10^{-4}	7.746×10^{-5}	0

- definition study report, arXiv preprint arXiv:2402.07571 (2024).
- [2] S. Sato, S. Kawamura, M. Ando, T. Nakamura, K. Tsubono, A. Araya, I. Funaki, K. Ioka, N. Kanda, S. Moriwaki, *et al.*, The status of decigo, in *Journal of Physics: Conference Series*, Vol. 840 (IOP Publishing, 2017) p. 012010.
- [3] M. Ando, S. Kawamura, N. Seto, S. Sato, T. Nakamura, K. Tsubono, T. Takashima, I. Funaki, K. Numata, N. Kanda, *et al.*, Decigo and decigo pathfinder, *Classical and Quantum Gravity* **27**, 084010 (2010).
- [4] S. Kawamura, M. Ando, N. Seto, S. Sato, T. Nakamura, K. Tsubono, N. Kanda, T. Tanaka, J. Yokoyama, I. Funaki, *et al.*, The japanese space gravitational wave antenna: Decigo, *Classical and Quantum Gravity* **28**, 094011 (2011).
- [5] W.-H. Ruan, Z.-K. Guo, R.-G. Cai, and Y.-Z. Zhang, Taiji program: Gravitational-wave sources, *Int. J. Mod. Phys. A* **35**, 2050075 (2020).
- [6] W.-R. Hu and Y.-L. Wu, The taiji program in space for gravitational wave physics and the nature of gravity (2017).
- [7] J. Luo *et al.*, Tianqin: a space-borne gravitational wave detector, *Classical Quantum Gravity* **33**, 035010 (2016).
- [8] S. Liu, Y.-M. Hu, J.-d. Zhang, and J. Mei, Science with the tianqin observatory: Preliminary results on stellar-mass binary black holes, *Physical Review D* **101**, 103027 (2020).
- [9] J. Mei, Y.-Z. Bai, J. Bao, E. Barausse, L. Cai, E. Canuto, B. Cao, W.-M. Chen, Y. Chen, Y.-W. Ding, *et al.*, The tianqin project: Current progress on science and technology, *Progress of Theoretical and Experimental Physics* **2021**, 05A107 (2021).
- [10] W.-T. Ni, Astrod—an overview, *International Journal of Modern Physics D* **11**, 947 (2002).
- [11] W.-T. Ni, Astrod and astrod i—overview and progress, *International Journal of Modern Physics D* **17**, 921 (2008).
- [12] B. P. Abbott *et al.* (LIGO Scientific Collaboration and Virgo Collaboration), Observation of gravitational waves from a binary black hole merger, *Phys. Rev. Lett.* **116**, 061102 (2016).
- [13] B. Caron, A. Dominjon, C. Drezen, R. Flaminio, X. Grave, F. Marion, L. Massonnet, C. Mehmel, R. Morand, B. Mours, *et al.*, The virgo interferometer, *Classical and Quantum Gravity* **14**, 1461 (1997).
- [14] Y. Sekiguchi, K. Kiuchi, K. Kyutoku, and M. Shibata, Current status of numerical-relativity simulations in kyoto, *Progress of Theoretical and Experimental Physics* **2012**, 01A304 (2012).
- [15] B. P. Abbott, R. Abbott, T. Abbott, S. Abraham, F. Acernese, K. Ackley, C. Adams, V. Adya, C. Affeldt, M. Agathos, *et al.*, Prospects for observing and localizing gravitational-wave transients with advanced ligo, advanced virgo and kagra, *Living reviews in relativity* **23**, 3 (2020).
- [16] Z. Luo, Y. Wang, Y. Wu, W. Hu, and G. Jin, The taiji program: A concise overview, *Progress of Theoretical and Experimental Physics* **2021**, 05A108 (2020).
- [17] A. Dávila Álvarez, A. Knudtson, U. Patel, J. Gleason, H. Hollis, J. Sanjuan, N. Doughty, G. McDaniel, J. Lee, J. Leitch, *et al.*, A simplified gravitational reference sensor for satellite geodesy, *Journal of Geodesy* **96**, 70 (2022).
- [18] Z. Cai and J. Deng, Satellite architecture and preliminary in-orbit experiment of Taiji-1, *Int. J. Mod. Phys. A* **36**, 2140020 (2021).
- [19] G. Wang, W.-T. Ni, W.-B. Han, P. Xu, and Z. Luo, Alternative lisa-taiji networks, *Physical Review D* **104**, 024012 (2021).
- [20] K. J. Shuman and N. J. Cornish, Massive black hole binaries and where to find them with dual detector networks, *Physical Review D* **105**, 064055 (2022).
- [21] W.-H. Ruan, C. Liu, Z.-K. Guo, Y.-L. Wu, and R.-G. Cai, The lisa-taiji network, *Nature Astronomy* **4**, 108 (2020).
- [22] G. Orlando, M. Pieroni, and A. Ricciardone, Measuring parity violation in the stochastic gravitational wave background with the lisa-taiji network, *Journal of Cosmology and Astroparticle Physics* **2021** (03), 069.
- [23] M. Tinto and S. V. Dhurandhar, Time-delay interferometry, *Living Reviews in Relativity* **24**, 1 (2021).
- [24] Z. Luo, Z. Guo, G. Jin, Y. Wu, and W. Hu, A brief analysis to taiji: Science and technology, *Results in Physics* **16**, 102918 (2020).
- [25] P. Bender *et al.*, Lisa: a cornerstone mission for the observation of gravitational waves, System and technology study report ESA-SCI **11**, 2000 (2000).
- [26] P. Gath, W. Fichter, M. Kersten, and A. Schleicher, Drag free and attitude control system design for the lisa pathfinder mission, in *AIAA Guidance, Navigation, and Control Conference and Exhibit* (2004) p. 5430.
- [27] P. Gath, H. R. Schulte, D. Weise, and U. Johann, Drag free and attitude control system design for the lisa science mode, in *AIAA Guidance, Navigation and Control Conference and Exhibit* (2007) p. 6731.
- [28] S. Vidano, C. Novara, L. Colangelo, and J. Grzymisch, The lisa dfacs: A nonlinear model for the spacecraft dynamics, *Aerosp. Sci. Technol.* **107**, 106313 (2020).
- [29] M. Armano, H. Audley, J. Baird, P. Binetruy, M. Born, D. Bortoluzzi, E. Castelli, A. Cavalleri, A. Cesarini, A. Cruise, *et al.*, Calibrating the system dynamics of lisa pathfinder, *Physical Review D* **97**, 122002 (2018).

- [30] C. Reigber, H. Lühr, and P. Schwintzer, Champ mission status, *Advances in space research* **30**, 129 (2002).
- [31] S. Weil, *Gravity and grace* (U of Nebraska Press, 1997).
- [32] R. P. Kornfeld, B. W. Arnold, M. A. Gross, N. T. Dahya, W. M. Klipstein, P. F. Gath, and S. Bettadpur, Gracefo: the gravity recovery and climate experiment follow-on mission, *Journal of spacecraft and rockets* **56**, 931 (2019).
- [33] Z. Huang, S. Li, L. Cai, D. Fan, and L. Huang, Estimation of the center of mass of grace-type gravity satellites, *Remote Sens.* **14** (2022).
- [34] F. Wang, *Study on center of mass calibration and K-band ranging system calibration of the GRACE mission*, Ph.D. thesis, The University of Texas at Austin (2003).
- [35] F. Wang, S. Bettadpur, H. Save, and G. Kruizinga, Determination of center-of-mass of gravity recovery and climate experiment satellites, *J. Spacecr. Rockets* **47**, 371 (2010).
- [36] Y.-L. Wu *et al.* (Taiji Scientific Collaboration), China's first step towards probing the expanding universe and the nature of gravity using a space borne gravitational wave antenna, *Commun. Phys.* **4**, 34 (2021).
- [37] H. Zhang, P. Xu, Z. Ye, D. Ye, L.-E. Qiang, Z. Luo, K. Qi, S. Wang, Z. Cai, Z. Wang, J. Lei, and Y. Wu, A systematic approach for inertial sensor calibration of gravity recovery satellites and its application to taiji-1 mission, *Remote Sensing* **15**, 10.3390/rs15153817 (2023).
- [38] X. Wei, L. Huang, T. Shen, Z. Cai, and J. He, Calibration of the in-orbit center-of-mass of taiji-1, *Phys. Rev. D* **108**, 082001 (2023).
- [39] A.-N. Zhou, L. Cai, C.-Y. Xiao, D.-Y. Tan, H.-Y. Li, Y.-Z. Bai, Z.-B. Zhou, and J. Luo, Non-gravitational force measurement and correction by a precision inertial sensor of tianqin-1 satellite, *Classical and Quantum Gravity* **39**, 115005 (2022).
- [40] J. Luo, Y.-Z. Bai, L. Cai, B. Cao, W.-M. Chen, Y. Chen, D.-C. Cheng, Y.-W. Ding, H.-Z. Duan, X. Gou, C.-Z. Gu, D.-F. Gu, Z.-Q. He, S. Hu, Y. Hu, X.-Q. Huang, Q. Jiang, Y.-Z. Jiang, H.-G. Li, H.-Y. Li, J. Li, M. Li, Z. Li, Z.-X. Li, Y.-R. Liang, F.-J. Liao, Y.-C. Liu, L. Liu, P.-B. Liu, X. Liu, Y. Liu, X.-F. Lu, Y. Luo, J. Mei, M. Ming, S.-B. Qu, D.-Y. Tan, M. Tang, L.-C. Tu, C.-R. Wang, F. Wang, G.-F. Wang, J. Wang, L. Wang, X. Wang, R. Wei, S.-C. Wu, C.-Y. Xiao, M.-Z. Xie, X.-S. Xu, L. Yang, M.-L. Yang, S.-Q. Yang, H.-C. Yeh, J.-B. Yu, L. Zhang, M.-H. Zhao, and Z.-B. Zhou, The first round result from the tianqin-1 satellite, *Classical Quantum Gravity* **37**, 185013 (2020).
- [41] C. Liu, X. Wei, H. Zhang, Q. Deng, B. Liang, L. Qiang, P. Xu, K. Qi, and S. Wang, Design of in-orbit calibration scheme for scale factor and center-of-mass deviation of inertial sensor of taiji program for space gravitational wave detection, *ACTA PHYSICA SINICA* **74** (2025).
- [42] S.-A. Wang, H. Zhang, L. Cai, Z. Wang, and Y. An, Research on mass center identification for gravitational wave detection spacecraft with guaranteed laser link pointing accuracy, *Remote Sensing* **17**, 296 (2025).
- [43] L. I. S. Team *et al.*, Lisa unveiling a hidden universe, LISA Assessment Study Report, ESA/SRE **3** (2011).
- [44] F. Lupi, *Precise control of LISA with quantitative feedback theory*, Ph.D. thesis, Delft University of Technology Delft, The Netherlands (2019).
- [45] W. Brzozowski, D. Robertson, E. Fitzsimons, H. Ward, J. Keogh, A. Taylor, M. Milanova, M. Perreur-Lloyd, Z. Ali, A. Earle, *et al.*, The lisa optical bench: an overview and engineering challenges, *Space Telescopes and Instrumentation 2022: Optical, Infrared, and Millimeter Wave* **12180**, 237 (2022).
- [46] W. Brzozowski, D. Robertson, E. Fitzsimons, H. Ward, J. Keogh, A. Taylor, M. Milanova, M. Perreur-Lloyd, Z. Ali, A. Earle, *et al.*, The lisa optical bench: an overview and engineering challenges, *Space Telescopes and Instrumentation 2022: Optical, Infrared, and Millimeter Wave* **12180**, 237 (2022).
- [47] J. Bohan, L. Qifan, D. Zhaohui, Y. Xiaokui, X. Yuanqing, D. Li, H. Qinglei, Y. Chenglei, W. Pengcheng, G. Ming, *et al.*, A review on dfacs (i): System design and dynamics modeling, *Chinese Journal of Aeronautics* **37**, 92 (2024).
- [48] S. M. Merkwitz, K. E. Castellucci, S. V. Depalo, J. A. Generie, P. G. Maghami, and H. L. Peabody, Current lisa spacecraft design, *Journal of Physics Conference Series* **154**, 012021 (2009).
- [49] S. Vidano, M. Pagone, J. Grzymisch, V. Preda, and C. Novara, Drag-free and attitude control system for the lisa space mission: An h_∞ constrained decoupling approach, *IEEE Transactions on Control Systems Technology* **32**, 2149 (2024).
- [50] D.-W. Gu, P. H. Petkov, and M. M. Konstantinov, *Robust control design with MATLAB®* (Springer, 2005).
- [51] S. Boyd, L. El Ghaoui, E. Feron, and V. Balakrishnan, *Linear matrix inequalities in system and control theory* (SIAM, 1994).
- [52] M. Trifonov, K. F. Prochazka, and S. Krüger, Robust control of an input-redundant aircraft against atmospheric disturbances and actuator faults, *International Journal of Mechanical Engineering and Robotics Research* **8**, 905 (2019).
- [53] S. Vidano, M. Pagone, J. Grzymisch, V. Preda, and C. Novara, Drag-free and attitude control system for the lisa space mission: An H_∞ constrained decoupling approach, *IEEE Transactions on Control Systems Technology* **32**, 2149 (2024).
- [54] M. Viridis, *A Meteoroid Impact Recovery Control System for the LISA Gravitational Wave Observatory*, Ph.D. thesis, Politecnico di Torino (2021).
- [55] R. M. Georgevic, *Mathematical Model of the Solar Radiation Force and Torques Acting on the Components of a Spacecraft*, Tech. Rep. NASA TM 33-494 (Jet Propulsion Laboratory, 1971).
- [56] Z. Li and J. Zheng, Orbit determination for a space-based gravitational wave observatory, *Acta Astronautica* **185**, 170 (2021).
- [57] S. Vidano, C. Novara, M. Pagone, and J. Grzymisch, The lisa dfacs: Model predictive control design for the test mass release phase, *Acta Astronautica* **193**, 731 (2022).
- [58] Y. Chenglei, J. Bohan, D. Zhaohui, Y. Xiaokui, X. Yuanqing, D. Li, H. Qinglei, L. Qifan, W. Pengcheng, G. Ming, *et al.*, A review on dfacs (ii): Modeling and analysis of disturbances and noises, *Chinese Journal of Aeronautics* **37**, 120 (2024).
- [59] R. E. Kalman, A New Approach to Linear Filtering and Prediction Problems, *J. Basic Eng.* **82**, 35 (1960).
- [60] Q. Ge, T. Shao, Z. Duan, and C. Wen, Performance analysis of the kalman filter with mismatched noise covariances, *IEEE Transactions on Automatic Control* **61**, 4014 (2016).
- [61] Q. Ge, Y. Li, Y. Wang, X. Hu, H. Li, and C. Sun, Adaptive kalman filtering based on model parameter ratios, *IEEE Transactions on Automatic Control* **69**, 6230

- (2024).
- [62] A. P. Sage and G. W. Husa, Algorithms for sequential adaptive estimation of prior statistics, in *1969 IEEE Symposium on Adaptive Processes (8th) Decision and Control* (IEEE, 1969) pp. 61–61.
- [63] S. Akhlaghi, N. Zhou, and Z. Huang, Adaptive adjustment of noise covariance in kalman filter for dynamic state estimation, in *2017 IEEE power & energy society general meeting* (IEEE, 2017) pp. 1–5.
- [64] R. Mehra, Approaches to adaptive filtering, *IEEE Transactions on Automatic Control* **17**, 693 (1972).
- [65] K. A. Myers and B. D. Tapley, Adaptive sequential estimation for satellite tracking, *IEEE Transactions on Aerospace and Electronic Systems* **AES-12**, 418 (1976).
- [66] M. Song, R. Astroza, H. Ebrahimian, B. Moaveni, and C. Papadimitriou, Adaptive kalman filters for nonlinear finite element model updating, *Mechanical Systems and Signal Processing* **143**, 106837 (2020).